Monthly Notices
of the
ROYAL ASTRONOMICAL SOCIETY

Mon. Not. R. Astron. Soc. **400,** 134–146 (2009) doi:10.1111/j.1365-2966.2009.15462.x

Multiwavelength observations of the energetic GRB 080810: detailed mapping of the broad-band spectral evolution★

K. L. Page,[1]† R. Willingale,[1] E. Bissaldi,[2] A. de Ugarte Postigo,[3] S. T. Holland,[4,5,6] S. McBreen,[2,7] P. T. O'Brien,[1] J. P. Osborne,[1] J. X. Prochaska,[8] E. Rol,[1,9] E. S. Rykoff,[10] R. L. C. Starling,[1] N. R. Tanvir,[1] A. J. van der Horst,[11]‡ K. Wiersema,[1] B. Zhang,[12] F. J. Aceituno,[13] C. Akerlof,[14] A. P. Beardmore,[1] M. S. Briggs,[15] D. N. Burrows,[16] A. J. Castro-Tirado,[13] V. Connaughton,[15] P. A. Evans,[1] J. P. U. Fynbo,[17] N. Gehrels,[4] C. Guidorzi,[18,19] A. W. Howard,[20] J. A. Kennea,[16] C. Kouveliotou,[11] C. Pagani,[16] R. Preece,[15] D. Perley,[20] I. A. Steele[19] and F. Yuan[14]

[1]*Department of Physics & Astronomy, University of Leicester, University Road, Leicester LE1 7RH*
[2]*Max-Planck-Institut für Extraterrestrische Physik, 85748 Garching, Germany*
[3]*European Southern Observatory, Casilla 19001, Santiago 19, Chile*
[4]*NASA Goddard Space Flight Center, Greenbelt, MD 20771, USA*
[5]*Universities Space Research Association, 10211 Wincopin Circle, Suite 500, Columbia, MD 21044-3432, USA*
[6]*CRESST, Code 668.8, 8800 Greenbelt Road, Goddard Space Flight Centre, Greenbelt, MD 20771, USA*
[7]*School of Physics, University College Dublin, Dublin 4, Ireland*
[8]*Department of Astronomy and Astrophysics, UCO/Lick Observatory, University of California, Santa Cruz, CA 95064, USA*
[9]*Astronomical Institute Anton Pannekoek, University of Amsterdam, PO number 94249, 1090 GE, Amsterdam, the netherlands*
[10]*Physics Department, University of California at Santa Barbara, 2233B Broida Hall, Santa Barbara, CA 93106, USA*
[11]*NASA Marshall Space Flight Center, NSSTC, 320 Sparkman Drive, Huntsville, Alabama 35805, USA*
[12]*Department of Physics and Astronomy, University of Nevada, Las Vegas, NV 89154-4002, USA*
[13]*Instituto de Astrofísica de Andalucía (CSIC), Camino bajo de Huétor 50, PO Box 03004, E-18080 Granada, Spain*
[14]*University of Michigan, Randall Laboratory of Physics, 450 Church Street, Ann Arbor, MI 48109-1040*
[15]*University of Alabama in Huntsville, NSSTC, 320 Sparkman Drive, Huntsville, Alabama, 35805, USA*
[16]*Department of Astronomy and Astrophysics, Pennsylvania State University, 525 Davey Lab, University Park, PA 16802, USA*
[17]*Dark Cosmology Centre, Niels Bohr Institute, University of Copenhagen, Juliane Maries Vej 30, 2100 Copenhagen O, Denmark*
[18]*Physics Department, University of Ferrara, via Saragat 1, I-44100, Ferrara, Italy*
[19]*Astrophysics Research Institute, Liverpool John Moores University, Twelve Quays House, Egerton Wharf, Birkenhead CH41 1LD*
[20]*Department of Astronomy, University of California, Berkeley, CA 94720-3411, USA*

Accepted 2009 July 27. Received 2009 July 27; in original form 2009 May 22

ABSTRACT

GRB 080810 was one of the first bursts to trigger both *Swift* and the *Fermi* Gamma-ray Space Telescope. It was subsequently monitored over the X-ray and UV/optical bands by *Swift*, in the optical by Robotic Optical Transient Search Experiment (*ROTSE*) and a host of other telescopes, and was detected in the radio by the Very Large Array. The redshift of $z = 3.355 \pm 0.005$ was determined by Keck/High Resolution Echelle Spectrometer (HIRES) and confirmed by RTT150 and NOT. The prompt gamma/X-ray emission, detected over 0.3–10^3 keV, systematically softens over time, with $E_{\rm peak}$ moving from ∼600 keV at the start to ∼40 keV around 100 s after the trigger; alternatively, this spectral evolution could be identified with the blackbody temperature of a quasi-thermal model shifting from ∼60 to ∼3 keV over the same time interval. The first optical detection was made at 38 s, but the smooth, featureless profile of the full optical coverage implies that this is originated from the afterglow component, not from the pulsed/flaring prompt emission.

★This paper is dedicated to the memory of Professor Martin Turner, who sadly passed away during its writing. Martin was an influential figure in X-ray Astronomy and an excellent PhD supervisor. He will be greatly missed.

†E-mail: kpa@star.le.ac.uk

‡NASA postdoctoral program fellow.

Broad-band optical and X-ray coverage of the afterglow at the start of the final X-ray decay (∼8 ks) reveals a spectral break between the optical and X-ray bands in the range of 10^{15}–2×10^{16} Hz. The decay profiles of the X-ray and optical bands show that this break initially migrates blueward to this frequency and then subsequently drifts redward to below the optical band by $\sim 3 \times 10^5$ s. GRB 080810 was very energetic, with an isotropic energy output for the prompt component of 3×10^{53} and 1.6×10^{52} erg for the afterglow; there is no evidence for a jet break in the afterglow up to 6 d following the burst.

Key words: gamma-rays: bursts – X-rays: individual: GRB 080810.

1 INTRODUCTION

Gamma-ray bursts (GRBs) emit large amounts of energy across the full range of the electromagnetic spectrum, so obtaining panchromatic data allows a more thorough investigation of the processes involved. Even with the rapid slewing capability of *Swift* (Gehrels et al. 2004), few bursts have good, simultaneous multiband observations of the prompt emission. On rare occasions, a trigger on a precursor has allowed the X-ray Telescope and UV/Optical Telescope (XRT and UVOT; Burrows et al. 2005a; Roming et al. 2005) to be on target for (most of) the main event (e.g. GRB 060124 – Romano et al. 2006; GRB 061121 – Page et al. 2007), whereas, in about 10 per cent of *Swift*-detected GRBs, the duration of the burst has been such that the narrow-field instruments have been able to observe the tail-end of the prompt emission (e.g. GRB 070616 – Starling et al. 2008; GRB 060607A – Ziaeepour et al. 2008). Thus, whenever prompt emission is detected by more than just gamma-ray instruments, the GRB becomes potentially more interesting and informative, allowing models to be tested more rigorously.

In the case of GRB 080810, bright, highly variable emission detected by the Burst Alert Telescope (BAT; Barthelmy et al. 2005) continued for more than 100 s, with the XRT and UVOT on target and collecting data from ∼80 s (Page et al. 2008a); a bright source was detected in both the X-ray and optical bands. The gamma-ray emission was also observed by the *Fermi*[1] GRB Monitor (Meegan et al. 2008), making GRB 080810 one of the first GRBs to trigger both it and the BAT; Konus–Wind also detected this burst (Sakamoto et al. 2008b). Many telescopes reported the detection of the optical afterglow (see Page et al. 2008b for a summary) while Prochaska et al. (2008) announced a tentative redshift of $z = 3.35$ using the Keck/HIRES spectrograph, which was then confirmed by RTT150 (Burenin et al. 2008) and Nordic Optical Telescope (NOT; de Ugarte Postigo et al. 2008a). The Very Large Array also detected the radio afterglow at 8.46 GHz (Chandra & Frail 2008) 3–4 d after the burst.

Section 2 presents the observations and preliminary results, covering the gamma-ray (Section 2.1), X-ray (Section 2.2) and optical (Section 2.3) bands. Section 3 discusses the redshift determination (Section 3.1), using a thermal interpretation to provide an alternative spectral fit (Section 3.2) and the multiwavelength, broad-band modelling (Section 3.3). The conclusions are given in Section 4. Throughout this paper, we follow the convention of $F_{\nu,t} \propto \nu^{-\beta} t^{-\alpha}$ (photon spectral index $\Gamma = \beta + 1$), where $F_{\nu,t}$ is the flux density, ν is the observed frequency and t is the time since the onset of the burst. Errors are given at 90 per cent confidence unless otherwise stated.

[1] Formerly known as Gamma-ray Large Area Space Telescope (GLAST).

2 OBSERVATIONS AND ANALYSES

Swift and *Fermi* both triggered on GRB 080810 at 13:10:12 UT on 2008 August 10 (this time is used as T_0 throughout the paper), with the *Swift*-XRT and UVOT detecting the afterglow as soon as they were on target. The best *Swift* position is that determined from the UVOT refined analysis (Holland & Page 2008): RA = $23^{\rm h}47^{\rm m}10\overset{\rm s}{.}48$, Dec. = $+00^\circ 19' 11\overset{''}{.}3$ (J2000; estimated uncertainty of 0.6 arcsec), consistent with the Robotic Optical Transient Search Experiment III (*ROTSE*-III; Rykoff 2008) and NOT (de Ugarte Postigo et al. 2008a) localizations.

2.1 Gamma-rays

GRB 080810 was clearly detected by the *Swift*–BAT (Sakamoto et al. 2008a) over all energy bands (Fig. 1), although the emission above about 100 keV is weaker than at the lower energies. The T_{90} (15–150 keV) is 108 ± 5 s (estimated error including systematics); the fluence over this time is 4.2×10^{-6} erg cm^{-2}. The slow rise of the emission, over which there are multiple, overlapping peaks, started about 20 s (observer's frame) before the trigger.

Konus–Wind also detected GRB 080810, but observed the burst in waiting mode (Sakamoto et al. 2008b), meaning only 3-channel spectra were available, covering 20 keV to 1 MeV.

The *Fermi* Gamma-Ray Burst Monitor (GBM) (von Kienlin et al. 2004; Meegan et al. 2009) triggered on the burst as well (Meegan et al. 2008), identifying the same pulses as did the BAT (Fig. 1). Unfortunately, the burst was outside the field of view of the Large Area Telescope (LAT), which is sensitive to higher energy photons than GBM (0.02–300 GeV, compared to 8 keV–40 MeV).

The *Fermi*–GBM NaI detectors provide similar T_{90} estimates to that measured by the BAT, while the higher energy Bismuth Germanate scintillators (BGO) durations are shorter; values are given in Table 1. This is a consequence of the hard-to-soft evolution (see, e.g. Table 2), combined with the different sensitivities of the instruments.

Time-sliced spectra from both the BAT and *Fermi* (NaI and BGO) detectors, covering 0–10, 10–20, 20–27, 40–53 and 100–106 s after the trigger, were fitted with single and cut-off power laws and the results given in Table 2; the thermal fits are discussed in Section 3.2. The useful energy ranges for the BAT, NaI and BGO spectral fitting are 15–150, 8–1000 and 200–40 000 keV, respectively. The spectra and models were extensively tested in both XSPEC (Arnaud 1996) and the *Fermi* software package RMFIT (Mallozzi, Preece & Briggs 2005); these methods provided consistent results and so the numbers given in this paper are those from XSPEC. Because BAT spectra are created already background-subtracted and have non-Poissonian

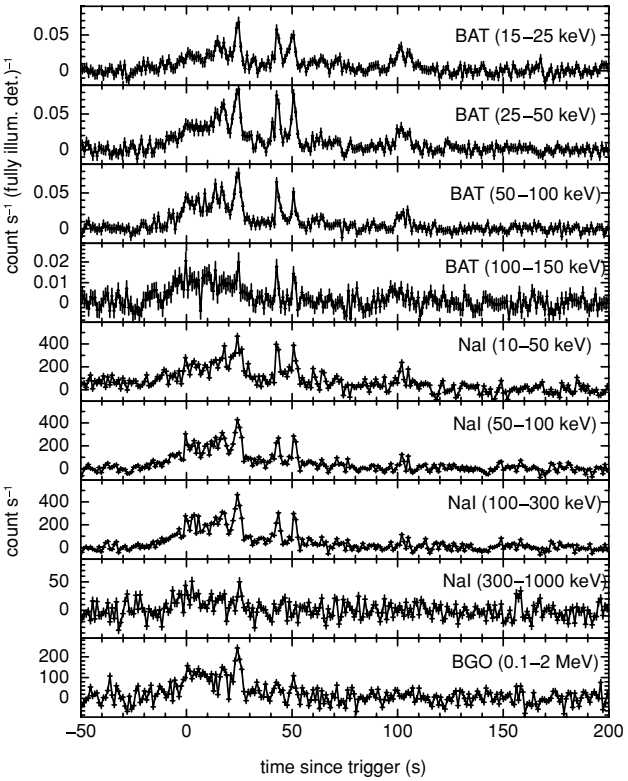

Figure 1. The *Swift*–BAT (top four panels) and *Fermi*–GBM (bottom five panels) light curves, over their standard energy bands. Note that the ordinate scale for the 100–150 keV BAT curve (fourth panel) and the 300–1000 keV NaI curve (eighth panel) are different from the lower energy bands because the emission was much weaker. The BGO light curve is shown down to 100 keV, but spectral analysis is performed only for data >200 keV. The *Swift* light curves are in units of count s^{-1} (fully illuminated detector)$^{-1}$, while the *Fermi* curves are count s^{-1}.

Table 1. T_{90} measurements over a range of energy bands. The longer duration at lower energies shows that the emission softened over time.

Instrument	Band (keV)	T_{90} (s)
Average		
Swift–BAT	15–150	108 ± 4
Fermi–NaI	10–1000	113 ± 2
Fermi–BGO	200–20 000	73 ± 7
Energy-sliced		
Swift–BAT	15–100	105 ± 4
Swift–BAT	100–150	55 ± 9
Fermi–NaI	10–50	107 ± 1
Fermi–NaI	50–100	81 ± 1
Fermi–NaI	100–300	73 ± 1

errors, Cash/Castor statistics cannot be used;[2] hence all results were obtained using χ^2 statistics.

Using the F-test, the Band function (Band et al. 1993) is not a statistical improvement over the simpler cut-off power law, with β, the higher energy index, unconstrained in each case. For the fits presented here, the normalizations of the GBM detectors were tied together at a value of 1.23 relative to the normalization of the BAT, which was itself fixed at unity. This constant of normalization for the GBM was determined by simultaneously fitting all five intervals of data, but allowing the other fit parameters to vary between the intervals. The cross-calibration between *Swift*–BAT and *Fermi*–GBM is discussed in Section 2.1.1.

Sakamoto et al. (2009) found a correlation between the photon index from a simple power-law fit to a BAT GRB spectrum and $E_{\rm peak}$, thus allowing an estimate of the peak energy from the limited BAT energy bandpass. The correlation for a source 15° off-axis (GRB 080810 was approximately 20° off-axis, so this is the closest of the relationships), $\log(E_{\rm peak}) = 3.184–0.793\Gamma$ (where $1.3 \leq \Gamma \leq 2.3$), was used to produce the estimated $E_{\rm peak}$ values given in Table 2 (marked as 'est.'); BAT slewed during the interval 12–64 s after the trigger, so $E_{\rm peak}$ was estimated for the last (100–106 s) spectrum using the on-axis approximation. The spectrum extracted for 0–10 s after the trigger has too hard a photon index to allow the use of this approximation, while 10–20 s is just consistent with the range. The 1σ spread of the relation has been included in the error estimation. These estimated peak energies are consistent with those found from jointly fitting the *Fermi* and *Swift* data, although the error bars on the measurements are very large.

The numbers show that the peak energy moves to lower values over time; this is demonstrated graphically in Fig. 2. The single power-law fits also show that Γ increased (softened) until at least 53 s. The spectrum from 100–106 s covers a flare in the XRT emission, which explains the harder (flatter) photon index (see Fig. 6).

Extracting simultaneous BAT and GBM spectra over $T_0 - 4$ – $T_0 + 26$ s (i.e. the brightest interval; Fig. 3), a cut-off power-law model is significantly better than a single power law, with $\Gamma = 1.05^{+0.07}_{-0.08}$ and $E_{\rm peak}$ estimated to be 569^{+290}_{-181} keV, corresponding to an isotropic energy release of $E_{\rm iso} \sim 3 \times 10^{53}$ erg (1 keV–10 MeV in the rest frame; $z = 3.355$ from Prochaska et al. 2008).

Fig. 4 plots the *Swift*–XRT and BAT and *Fermi*–NaI spectra between 100–106 s. There is only a tenuous detection in the BGO at this time, so that spectrum has not been included in the plot for clarity; it was, however, used in the fit to help constrain $E_{\rm peak}$.

Note that, in both of the above plots, the BAT data appear lower down the ordinate axis simply because of the way the normalizations are defined. Intercalibration between *Swift* and *Fermi* is discussed in Section 2.1.1.

2.1.1 Intercalibration

The intercalibration of the *Swift*–BAT and the *Fermi*–GBM is a work in progress and preliminary simulations were discussed by Stamatikos, Sakamoto & Band (2008); further results will be presented in Stamatikos et al. (in preparation). As mentioned in the previous section, the normalizations of the GBM detectors were all tied together for the current paper, finding a mean value of 1.23 ± 0.06 compared to a BAT value of unity. Allowing the normalizations to vary between the GBM detectors, while again simultaneously fitting all the data sets with a cut-off power law, produced the following relative constants: NaI $n7 = 1.24^{+0.09}_{-0.08}$, $n8 = 1.18 \pm 0.08$, $nb = 1.32^{+0.10}_{-0.09}$ and BGO $b1 = 1.88^{+0.31}_{-0.27}$, where, as before, the BAT constant was fixed to unity. Thus, the GBM detectors agree quite well, with a typical discrepancy of $\lesssim$20 per cent.

2.2 X-rays

Swift–XRT identified and centroided on an uncatalogued X-ray source in a 2.5 s Image Mode frame, 76 s after the BAT trigger. The source was bright enough such that the XRT stayed in

[2] http://heasarc.gsfc.nasa.gov/docs/xanadu/xspec/manual/XSappendixCash.html

Table 2. Power law (PL), cut-off power law (CutPL) and quasi-thermal (PL+Therm) fits to time-sliced spectra from GBM and BAT; the *Fermi* NaI n7, n8, nb and BGO b1 detectors were fitted simultaneously each time. The $E_{\rm peak}$ for the BAT single power-law fits are estimated from the relation given by Sakamoto et al. (2009); see text for details.

Time (s since trigger)	Detectors	Model	Γ	$E_{\rm peak}$ (keV)	BB kT (keV)	χ^2/d.o.f.
0–10	BAT	PL	0.92 ± 0.13	–	–	66/56
0–10	GBM	PL	1.48 ± 0.04	–	–	582/488
0–10	GBM	CutPL	$1.06^{+0.13}_{-0.17}$	807^{+1113}_{-470}	–	509/485
0–10	GBM+BAT	PL	1.43 ± 0.03	–	–	694/544
0–10	GBM+BAT	CutPL	$0.95^{+0.12}_{-0.13}$	602^{+537}_{-252}	–	580/543
0–10	GBM+BAT	PL+Therm	1.63 ± 0.11	–	62 ± 9	597/542
10–20	BAT	PL	1.24 ± 0.10	159^{+738}_{-92} (est.)	–	30/56
10–20	GBM	PL	1.56 ± 0.04	–	–	568/486
10–20	GBM	CutPL	$1.07^{+0.15}_{-0.18}$	346^{+378}_{-160}	–	505/485
10–20	GBM+BAT	PL	1.53 ± 0.03	–	–	622/544
10–20	GBM+BAT	CutPL	$1.09^{+0.11}_{-0.12}$	353^{+275}_{-139}	–	536/543
10–20	GBM+BAT	PL+Therm	$1.69^{+0.10}_{-0.09}$	–	46^{+8}_{-8}	553/542
20–27	BAT	PL	1.23 ± 0.11	162^{+757}_{-99} (est.)	–	39/56
20–27	GBM	PL	1.53 ± 0.04	–	–	538/486
20–27	GBM	CutPL	$1.11^{+0.13}_{-0.14}$	434^{+425}_{-190}	–	476/485
20–27	GBM+BAT	PL	1.50 ± 0.03	–	–	596/544
20–27	GBM+BAT	CutPL	$1.12^{+0.10}_{-0.11}$	452^{+356}_{-176}	–	516/543
20–27	GBM+BAT	PL+Therm	$1.64^{+0.09}_{-0.08}$	–	53^{+11}_{-9}	538/542
40–53	BAT	PL	1.60 ± 0.10	82^{+160}_{-32} (est.)	–	60/56
40–53	GBM	PL	1.69 ± 0.06	–	–	620/486
40–53	GBM	CutPL	$1.27^{+0.23}_{-0.24}$	188^{+464}_{-114}	–	602/485
40–53	GBM+BAT	PL	1.67 ± 0.05	–	–	682/544
40–53	GBM+BAT	CutPL	$1.41^{+0.13}_{-0.16}$	230^{+538}_{-175}	–	664/543
40–53	GBM+BAT	PL+Therm	$1.78^{+0.15}_{-0.11}$	–	28^{+15}_{-9}	668/542
100–106	BAT	PL	1.71 ± 0.19	69^{+97}_{-52} (est.)	–	55/56
100–106	GBM	PL	$2.14^{+0.28}_{-0.23}$	–	–	600/486
100–106	GBM	CutPL	$0.99^{+0.83}_{-1.47}$	49^{+472}_{-49}	–	593/485
100–106	GBM+BAT+XRT	PL	1.46 ± 0.02	–	–	904/585
100–106	GBM+BAT+XRT	CutPL	$1.05^{+0.07}_{-0.08}$	39^{+12}_{-9}	–	725/584
100–106	GBM+BAT+XRT	PL+Therm	1.46 ± 0.03	–	$2.6^{+0.4}_{-0.7}$	797/583

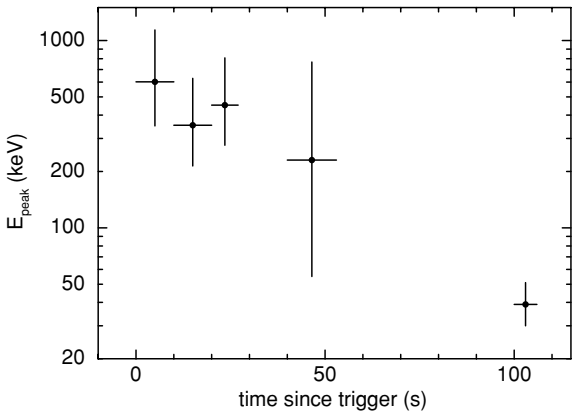

Figure 2. $E_{\rm peak}$, measured from joint *Fermi–Swift* fits, moves to lower energies with time.

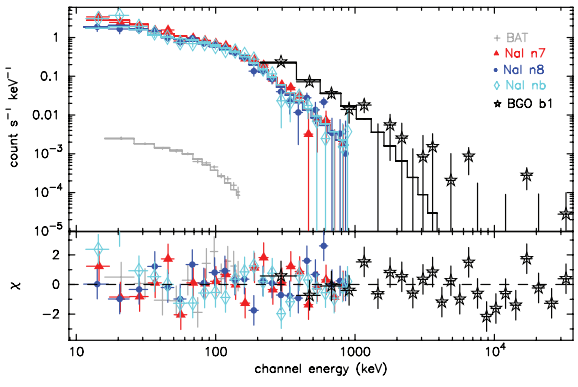

Figure 3. GBM and BAT spectra covering −4 to 26 s over the trigger. The residuals are plotted in terms of sigma, with error bars of 1σ.

Windowed Timing (WT) mode throughout the first orbit, which ended about 460 s after the trigger. The WT data showed two large flares, with smaller peaks superimposed (Fig. 5), with an underlying decay of $\alpha = 1.05^{+0.17}_{-0.14}$.

By the time of the second orbit, the source had faded sufficiently that data could be collected in Photon Counting (PC) mode. The 'canonical' X-ray light curve identified from *Swift* bursts (Nousek et al. 2006; Zhang et al. 2006) follows a steep-shallow-normal pattern (possibly with a later jet-break) and, while not all bursts

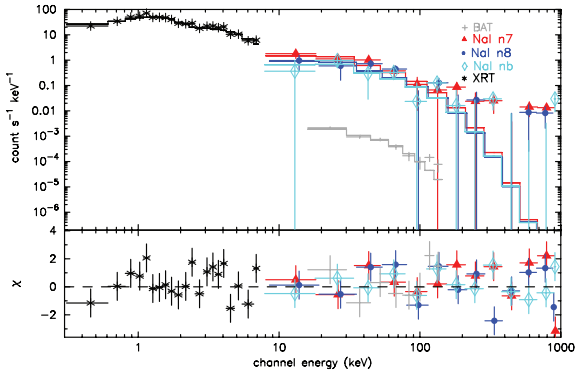

Figure 4. *Fermi*–GBM, BAT and XRT spectra covering 100–106 s after the trigger. The residuals are plotted in terms of sigma, with error bars of 1σ.

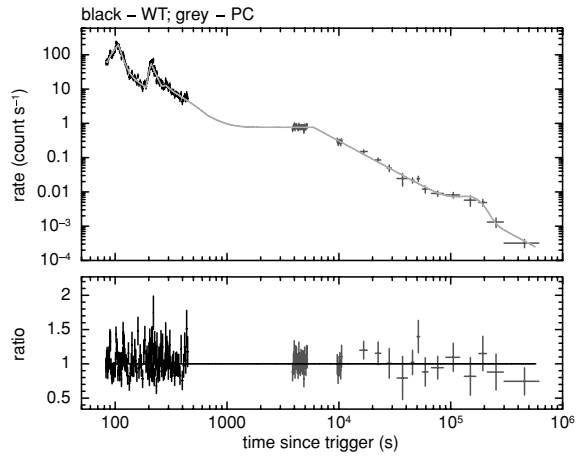

Figure 5. 0.3–10 keV X-ray light curve. The decay has been fitted with a doubly broken power law and overlying flare/Gaussian components (described in the text). The lower panel shows the ratio between the data and the model.

show all these components (Evans et al. 2009), in this case the first PC orbit could be identified as the end of the shallow plateau phase. *Swift* is in a low-Earth orbit, so can only observe a given target for a maximum of about 1.5–2 ks per 96 min revolution, leading to orbital gaps in the data. Because of these intervals of no data, the start time of the plateau in the GRB 080810 X-ray light curve is very uncertain. Nevertheless, a flattening in the decay at this time was a statistical improvement. The best-fitting parameters obtained by fitting the complete light curve with a doubly broken power law (plus flare components, as shown in Fig. 5) are given in Table 3; because of the limited data, the plateau phase was poorly constrained. There was a deviation from the late-time power-law decay around ∼150 ks, when the X-ray emission briefly rebrightened.

The early flares (almost certainly due to the continuation of the prompt emission component) are well fitted with Fast Rise Exponential Decay-like (FRED) profiles, while the deviation around 10^5 s can be equally well-modelled by either a FRED-like profile or a Gaussian. However, it should be noted that the data are much better sampled at early times, so the shape of the later flare is more uncertain. A model comprising a power-law decay with six superimposed, sometimes over-lapping flares (at $\sim T_0 + 91$, 102, 107, 118, 210 and 281 s; the strongest peaks are those at 102 and 210 s) provides a good fit to the WT data, with each flare component being statistically significant. There are also additional deviations, but adding further flares to the model does not improve the fit.

Table 3. The doubly broken power-law model fitted to the decay continuum; the 'plateau' phase is poorly constrained. A number of flare components are also required to give a good fit. The three main early flares peak at 107, 210 and 281 s; a later rebrightening occurs around 150 ks. See text for more details.

Parameter	Value
α_1	$1.05^{+0.17}_{-0.14}$
$T_{\rm b,1}$	2679^{+1677}_{-1335} s
α_2	$-0.03^{+0.57}_{-0.58}$
$T_{\rm b,2}$	5909^{+969}_{-518} s
α_3	$1.76^{+0.10}_{-0.08}$

Including these six burst components at early times, and a Gaussian to model the later-time rebrightening, we obtain χ^2/d.o.f. = 134/130 ($\chi^2_\nu = 1.03$).

The spectrum of the plateau orbit ($\sim T_0 + 4$–5 ks) can be modelled with a power law of $\Gamma = 1.95 \pm 0.07$ absorbed by the Galactic column of $N_{\rm H} = 3.28 \times 10^{20}$ cm^{-2}. After the temporal break, the photon index is $\Gamma = 2.00 \pm 0.09$, so there is no sign of spectral evolution at this point. A spectrum extracted just for the late-time 'bump' in the light curve is also consistent with these values, with $\Gamma = 1.99^{+0.28}_{-0.24}$. The lack of measured intrinsic absorption is not unusual for bursts at medium to high redshift (see, e.g. Grupe et al. 2007) and is also consistent with the optical data (see Section 3.1).

2.3 Optical

Swift–UVOT detected a bright optical afterglow in the *v*, *b* and *white* filters (Holland & Page 2008); the non-detection in *u* and the UV filters (∼4 ks after the trigger) is consistent with the redshift of 3.355.

ROTSE-III (Akerlof et al. 2003), at the Siding Spring Observatory in Australia, imaged GRB 080810 35 s after the burst (Rykoff 2008), detecting a counterpart which brightened for about 30 s, before fading first with a shallow decay, then with a steeper slope. These unfiltered magnitudes have been normalized to the *R* band for subsequent analysis; the method is described by Rykoff et al. (2009).

A target-of-opportunity program was triggered on the Keck telescopes to obtain HIRES spectroscopy (Vogt et al. 1994) of the afterglow of GRB 080810, with the observations beginning around 37 min after the trigger (Prochaska et al. 2008); these data showed the redshift of the burst to be $z \sim 3.35$ (see Section 3.1).

The NOT observations (de Ugarte Postigo et al. 2008a) began 10.59 h after the burst, providing confirmation of the redshift. This was followed by observations with the 1.5-m Observatorio de Sierra Nevada (OSN; de Ugarte Postigo, Aceituno & Castro-Tirado 2008b) telescope and the 1.54-m Danish telescope at La Silla, Chile (Thöne, de Ugarte Postigo & Liebig 2008).

Data from the Faulkes Telescopes North & South, the Liverpool Telescope (LT; Guidorzi, Steele & Tanvir 2008; Guidorzi, Bersier & Tanvir 2008), the Isaac Newton Telescope (INT/WFC) and the NOT (de Ugarte Postigo et al. 2008a) were reduced in standard fashion, including bias subtraction and flat-fielding; i'-band observations were additionally defringed. Seeing-matched aperture photometry was performed using the Image Reduction and

Analysis Facility (IRAF).[3] Absolute calibration was performed using the Sloan Digital Sky Survey (SDSS; Adelman-McCarthy et al. 2008), with conversion to Johnson–Cousins.[4]

All the optical data included in this paper are listed in Table 4, including data from KANATA, obtained from the Gamma-Ray Bursts Coordinates Network (GCN; Ikejiri et al. 2008). These magnitudes have not been corrected for Galactic extinction (although the fluxes used later have been).

The *white* and v-band UVOT data are plotted in the second panel of Fig. 6, with the *ROTSE*-III data in the third. The UVOT *white* data have been normalized to align with the v band at 180–190 s (shown by the vertical line in the plot). There is an indication that the *white* magnitude increases around the same time as the first flare seen by the XRT, but this is only significant at the 1.5σ level. After this time, the UVOT data appear to follow a smooth decline, with no indication of a brightening at the time of the second X-ray flare (210 s after the trigger).

The *ROTSE*-III data show a clear $\sim$1 mag brightening between $T_0 + 40$ s and $T_0 + 60$ s. Although there is apparent structure in the light curve between $\sim$120–260 s, the limiting magnitudes were shallow at these times (caused by cloud cover), meaning these variations are not very significant.

The lack of obvious flaring in the optical coincident with the X-ray flares implies that this emission is strongly dominated by the afterglow and has very little (if any) contribution from the prompt emission.

3 DISCUSSION

In this section, we first present details about how the redshift was determined from the Keck data, then an alternative model for the prompt data and finally discuss the panchromatic observations and what can be learnt from them.

3.1 Redshift determination

Fig. 7 presents a Keck velocity plot for a series of transitions corresponding to a $\delta v \approx 1300$ km s^{-1} interval around $z \approx 3.355$. The top panel shows a pair of broad transitions (centred at $v \approx 0$ and $+700$ km s^{-1}) which mark the reddest Lyα features detected in the spectrum. Blueward of these data is a series of Lyα features which correspond to the intergalactic medium (IGM) at $z < 3.35$. The termination of the IGM establishes a rough redshift (conservatively, a lower limit) for the GRB host galaxy, that is $z_{\rm GRB} \approx 3.355$.

Fig. 7 reveals that each of these Lyα features also show corresponding metal-line transitions of Si II, C II (both around 0, 50 and 760 km s^{-1}) and C IV (from -80 to $+80$ km s^{-1} and $+580$ to almost $+800$ km s^{-1}). Also detected is absorption from O I, Si IV, Al II and a number of other ions (not shown in the plot). However, it is only the gas at $v \approx 0$ km s^{-1} (i.e. $z \approx 3.351$) that shows significant absorption from fine-structure levels of the Si II, C II and O I ions/atoms. Absorption from these fine-structure levels (e.g. Si II* 1264) is a strong signature of gas near the GRB afterglow because the afterglow itself is the excitation mechanism (Prochaska, Chen

[3] IRAF is distributed by the National Optical Astronomy Observatories, which are operated by the Association of Universities for Research in Astronomy, Inc., under cooperative agreement with the National Science Foundation.
[4] Following http://www.sdss.org/dr6/algorithms/sdssUBVRITransform.html#Lupton2005

Table 4. Optical data obtained for GRB 080810; errors are at the 1σ level. No correction for Galactic extinction has been made. FTS/N = Faulkes Telescope South/North; NOT = Nordic Optical Telescope; OSN = Observatorio de Sierra Nevada; DK = Danish telescope at La Silla; LT = Liverpool Telescope; INT/WFC = Isaac Newton Telescope/Wide Field Camera. KANATA data were taken from Ikejiri et al. (2008). The UVOT u, b and v filters are close to the standard *UBV* system. (Poole et al. 2008). Errors are at the 1σ level.

Filter	Mag.	Time (s since burst)	Exp. time (s)	Telescope
I	19.36 ± 0.09	47863	300	1.5m-OSN
I	19.34 ± 0.08	50548	300	1.5m-OSN
I	19.42 ± 0.13	52581	300	1.5m-OSN
I	19.51 ± 0.08	53558	300	1.5m-OSN
i	19.91 ± 0.03	52186	1800	LT
i	20.67 ± 0.06	124762	1800	LT
i	21.11 ± 0.06	174122	1500	FTN
i	21.08 ± 0.05	177534	1800	FTN
i	21.54 ± 0.06	224122	1800	LT
i	21.60 ± 0.07	242905	1800	FTN
i	21.66 ± 0.07	261896	1800	FTN
i	21.90 ± 0.09	311386	900	INT/WFC
i	22.63 ± 0.10	401674	1200	INT/WFC
R	15.95 ± 0.12	3320	300	FTS
R	16.30 ± 0.12	3697	180	FTS
R	16.27 ± 0.12	3886	180	FTS
R	16.46 ± 0.12	4075	180	FTS
R	16.48 ± 0.12	4263	180	FTS
R	16.66 ± 0.12	4453	180	FTS
R	16.39 ± 0.12	4712	300	FTS
R	16.97 ± 0.12	5689	300	FTS
R	16.84 ± 0.12	6624	300	FTS
R	16.97 ± 0.12	7422	300	FTS
R	21.55 ± 0.09	244918	1800	FTN
R	21.56 ± 0.06	265404	1800	FTN
R	19.31 ± 0.07	38117	120	NOT
R	19.66 ± 0.07	43110	300	1.5m-OSN
R	19.78 ± 0.04	47548	300	1.5m-OSN
R	19.81 ± 0.06	48212	300	1.5m-OSN
R	19.75 ± 0.04	48868	300	1.5m-OSN
R	19.78 ± 0.06	50016	300	1.5m-OSN
R	19.81 ± 0.06	50215	300	1.5m-OSN
R	19.76 ± 0.05	50884	300	1.5m-OSN
R	19.83 ± 0.05	51559	300	1.5m-OSN
R	19.85 ± 0.06	52255	300	1.5m-OSN
R	19.89 ± 0.06	52916	300	1.5m-OSN
R	19.83 ± 0.08	53879	300	1.5m-OSN
R	19.65 ± 0.06	54530	300	1.5m-OSN
R	20.76 ± 0.09	140260	900	1.5m-OSN
R	22.44 ± 0.31	419360	3000	1.5m-DK
R	22.95 ± 0.38	497928	5400	1.5m-DK
R	19.02 ± 0.05	37420	1800	1.5m-DK
r	20.18 ± 0.01	55987	1800	LT
r	20.96 ± 0.02	142301	1800	LT
r	21.72 ± 0.04	216691	2100	LT
r	22.10 ± 0.09	307411	780	INT/WFC
r	22.59 ± 0.06	395798	5700	INT/WFC
Unfilt	13.70 ± 0.03	38	5	*ROTSE*-III
Unfilt	13.00 ± 0.03	52	5	*ROTSE*-III
Unfilt	12.79 ± 0.03	67	5	*ROTSE*-III
Unfilt	12.78 ± 0.04	81	5	*ROTSE*-III
Unfilt	12.81 ± 0.03	95	5	*ROTSE*-III
Unfilt	12.63 ± 0.12	124	5	*ROTSE*-III
Unfilt	12.84 ± 0.11	138	5	*ROTSE*-III
Unfilt	13.06 ± 0.19	152	5	*ROTSE*-III
Unfilt	12.94 ± 0.03	173	20	*ROTSE*-III

Table 4 – *continued*

Filter	Mag.	Time (s since burst)	Exp. time (s)	Telescope
Unfilt	12.87 ± 0.19	261	20	*ROTSE*-III
Unfilt	13.65 ± 0.10	386	20	*ROTSE*-III
Unfilt	13.76 ± 0.03	444	20	*ROTSE*-III
Unfilt	13.91 ± 0.03	493	60	*ROTSE*-III
Unfilt	14.06 ± 0.04	562	60	*ROTSE*-III
Unfilt	14.14 ± 0.16	631	60	*ROTSE*-III
Unfilt	14.36 ± 0.07	700	60	*ROTSE*-III
Unfilt	14.37 ± 0.07	770	60	*ROTSE*-III
Unfilt	14.49 ± 0.06	839	60	*ROTSE*-III
Unfilt	14.66 ± 0.13	908	60	*ROTSE*-III
Unfilt	14.77 ± 0.14	977	60	*ROTSE*-III
Unfilt	14.70 ± 0.07	1046	60	*ROTSE*-III
Unfilt	14.86 ± 0.04	1115	60	*ROTSE*-III
Unfilt	15.16 ± 0.03	1504	682	*ROTSE*-III
Unfilt	15.75 ± 0.05	2196	684	*ROTSE*-III
Unfilt	15.79 ± 0.1	2823	552	*ROTSE*-III
Unfilt	16.45 ± 0.05	4438	682	*ROTSE*-III
Unfilt	16.83 ± 0.05	5129	682	*ROTSE*-III
Unfilt	16.94 ± 0.04	5821	682	*ROTSE*-III
Unfilt	17.10 ± 0.06	6512	682	*ROTSE*-III
Unfilt	17.29 ± 0.04	7203	682	*ROTSE*-III
Unfilt	17.42 ± 0.06	7898	690	*ROTSE*-III
Unfilt	17.39 ± 0.15	9298	690	*ROTSE*-III
V	20.27 ± 0.07	49190	300	1.5m-OSN
V	20.33 ± 0.08	51228	300	1.5m-OSN
V	20.35 ± 0.09	53239	300	1.5m-OSN
V	20.44 ± 0.11	54203	300	1.5m-OSN
V	13.7 ± 0.1[a]	390	33	KANATA
v	13.73 ± 0.08	196	10	UVOT
v	13.81 ± 0.08	206	10	UVOT
v	13.80 ± 0.08	216	10	UVOT
v	13.74 ± 0.08	226	10	UVOT
v	13.89 ± 0.08	236	10	UVOT
v	13.83 ± 0.08	246	10	UVOT
v	13.95 ± 0.08	256	10	UVOT
v	13.74 ± 0.08	266	10	UVOT
v	13.91 ± 0.08	276	10	UVOT
v	14.04 ± 0.08	286	10	UVOT
v	13.98 ± 0.08	296	10	UVOT
v	13.93 ± 0.08	306	10	UVOT
v	14.14 ± 0.08	316	10	UVOT
v	14.00 ± 0.08	326	10	UVOT
v	14.27 ± 0.09	336	10	UVOT
v	14.14 ± 0.08	346	10	UVOT
v	14.09 ± 0.08	356	10	UVOT
v	14.12 ± 0.08	366	10	UVOT
v	14.21 ± 0.09	376	10	UVOT
v	14.28 ± 0.09	386	10	UVOT
v	14.27 ± 0.09	396	10	UVOT
v	14.16 ± 0.08	406	10	UVOT
v	14.49 ± 0.09	416	10	UVOT
v	14.39 ± 0.09	426	10	UVOT
v	14.32 ± 0.09	436	10	UVOT
v	14.46 ± 0.09	446	10	UVOT
v	14.50 ± 0.10	456	10	UVOT
v	17.53 ± 0.10	5148	197	UVOT
v	21.10 ± 0.49	63077	1079	UVOT
v	20.79 ± 0.44	103938	777	UVOT
v	22.05 ± 0.49	303764	5964	UVOT
B	21.14 ± 0.12	49887	300	1.5m-OSN
B	21.23 ± 0.13	51901	300	1.5m-OSN
b	17.89 ± 0.08	4532.3	197	UVOT
b	20.28 ± 0.16	27235	569	UVOT

Table 4 – *continued*

Filter	Mag.	Time (s since burst)	Exp. time (s)	Telescope
b	21.45 ± 0.32	56302	867	UVOT
b	21.83 ± 0.47	79387	778	UVOT
b	21.60 ± 0.38	102520.4	831	UVOT
b	22.55 ± 0.52	164312	2162	UVOT
white	14.87 ± 0.10	90	10	UVOT
white	14.78 ± 0.11	100	10	UVOT
white	14.68 ± 0.12	110	10	UVOT
white	14.71 ± 0.12	120	10	UVOT
white	14.89 ± 0.10	130	10	UVOT
white	14.83 ± 0.11	140	10	UVOT
white	14.90 ± 0.10	150	10	UVOT
white	14.93 ± 0.10	160	10	UVOT
white	14.93 ± 0.10	170	10	UVOT
white	14.93 ± 0.10	180	10	UVOT

[a]Taken from Ikejiri et al. (2008).

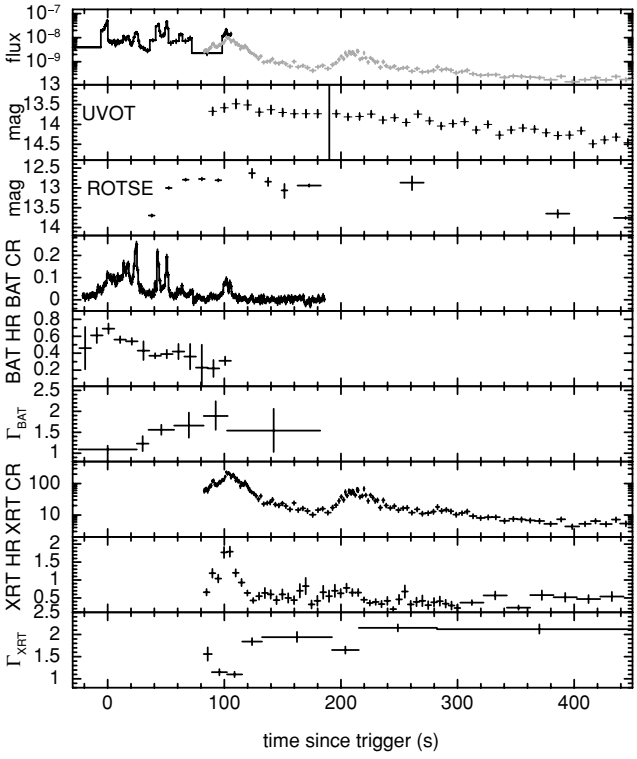

Figure 6. From top to bottom: the joint BAT–XRT flux light curve, in erg cm^{-2} s^{-1} over 0.3–10 keV (black histogram – BAT; grey crosses – XRT), during the first orbit; the *white* and *v*-band UVOT light curve (the data before the vertical line are *white*, normalized to align with the *v* band; afterwards – *v*); unfiltered *ROTSE*-III light curves; the BAT 15–150 keV light curve; the BAT hardness ratio over (50–150 keV)/(15–50 keV); time-sliced spectral fits to the BAT data; the XRT light curve; the XRT hardness ratio over (1.5–10 keV)/(0.3–1.5 keV); time-sliced spectral fits to the XRT data.

& Bloom 2006). Therefore, we are inclined to associate the GRB with the redshift of this material. Under this hypothesis, the gas at $v \approx +700$ km s^{-1} might be considered a neighbouring galaxy with a very large, positive peculiar velocity.

An alternative hypothesis is that the gas at $v \approx +700$ km s^{-1} (i.e. $z \approx 3.36$) marks the ambient interstellar medium of the host galaxy and that the material at $v \approx 0$ km s^{-1} is due to a fast outflow of material near the GRB afterglow. This hypothesis is challenged

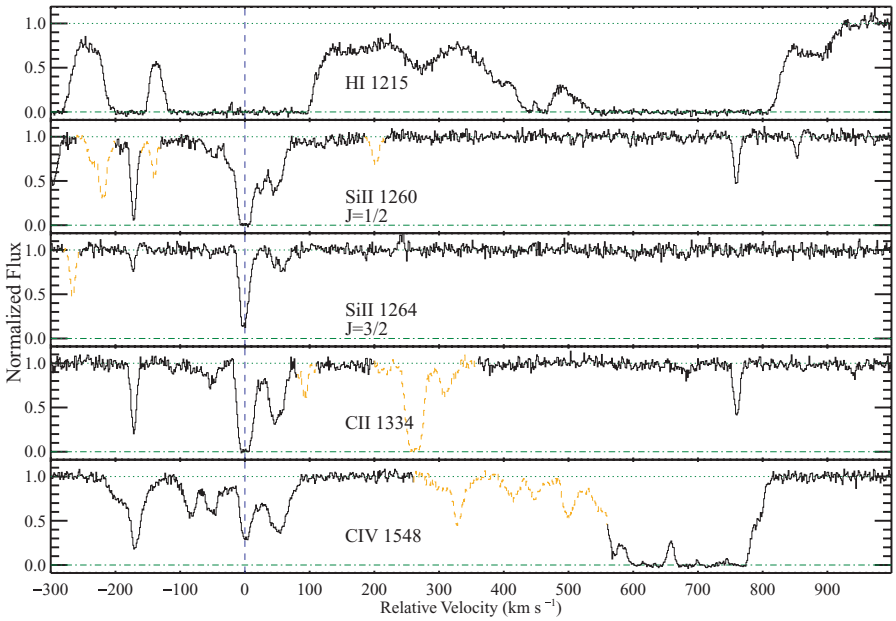

Figure 7. Keck/HIRES velocity plots for a subset of the transitions detected at $z \approx z_{\rm GRB}$. In the figure $v = 0$ km s^{-1} corresponds to an arbitrary $z = 3.35104$ and orange-dashed lines indicate blends with coincident features. Within the velocity interval shown, we detect two strong (broad) Lyα lines centred at $v = 0$ km s^{-1} and $v \approx +700$ km s^{-1} and corresponding metal-line absorption, including very strong C IV absorption. These Lyα lines are the reddest observed in the afterglow and we conclude that one (or both) are associated with the GRB host galaxy. Both complexes also show significant resonance, low-ion absorption from Si II and C II ions, but only the gas at $z \approx 3.35$ shows significant absorption from fine-structure levels of these ions.

by the fast wind speed required and the absence of fine-structure absorption in the Si II and C II gas at $v \approx +770$ km s^{-1}. An emission-line measurement of the host galaxy would be required to resolve these two possibilities and so we infer $z_{\rm GRB} = 3.355 \pm 0.005$.

Independent of the correct interpretation of the two systems, we can draw a few conclusions about the gas associated with GRB 080810. First, the total HI column is low relative to the mean value observed in GRB afterglow spectra (Jakobsson et al. 2006). For both Lyα lines, we set a conservative upper limit of $N_{\rm H\,I} < 10^{19.5}$ cm^{-2} based on the absence of strong damping wings. We also place a lower limit to the column density of the $z = 3.36$ absorber of $N_{\rm H\,I} > 10^{17.7}$ cm^{-2} based on Lyman limit absorption at $\lambda < 3976$ Å. Both systems show relatively weak low-ion absorption, consistent with the low $N_{\rm H\,I}$ values. In contrast, each shows very strong high-ion absorption, a characterstic of gas associated with GRB host galaxies (Prochaska et al. 2007). In agreement with this optical measurement, no absorption above the Galactic value was required when fitting the X-ray spectrum (Section 2.2).

We note in passing that GRBs 020813 (Barth et al. 2003) and 021004 (Fynbo et al. 2005) both showed similarly unusual absorption systems.

3.2 Thermal emission

Ryde (2004) and Ryde & Pe'er (2009) discuss the possibility that thermal emission may be ubiquitous in GRBs, fitting samples of spectra with a power-law-plus-blackbody model, and Lazzati, Morsony & Begelman (2009) present simulations of photospheric emission. Such thermal components may explain the hard early-time spectra which are inconsistent with synchrotron emission (Preece et al. 1998; Ghisellini, Celotti & Lazzati 2000; Savchenko & Neronov 2009). A similar quasi-thermal model was applied to the GRB 080810 gamma-ray spectra and the results are included in Table 2. In most of the spectra presented by Ryde & Pe'er (2009), a distinct break is seen in the temporal evolution of the blackbody temperature; this is not apparent in our data, though this may be related to the fact that our first spectrum spans $T_0 + 0$–10 s, and most of the breaks seen occur within 10 s of the burst. Following Pe'er et al. (2007), we have estimated the photospheric radius (the radius beyond which the outflow becomes optically thin) to be $\sim 2 \times 10^{11}\, Y_0$ cm, where Y_0 is the ratio between the fireball energy and the energy emitted in gamma-rays ($1 \lesssim Y_0 < 3$–5; see Pe'er et al. 2007). We also determine that the coasting Lorentz factor is $\sim 570\, Y_0^{1/4}$. These calculations assume that the blackbody temperature is the maximum measured (62 keV), since we do not see a break in the behaviour of the temperature. The ratio of the blackbody flux to the total flux over the gamma-ray band (10–10^4 keV) is 0.2 for this spectrum. With the exception of the spectrum after 100 s, where the blackbody is much weaker and cooler, this ratio remains between 0.1 and 0.2 for the spectra considered here. We do point out, however, that the fits systematically have a worse χ^2 than the cut-off power-law models.

3.3 Multiwavelength data

3.3.1 Broad-band modelling

The top panel of Fig. 6 shows the joint BAT–XRT flux light curve. The data were converted into 0.3–10 keV fluxes using power-law fits to time-sliced spectra; where there were simultaneous BAT and XRT detections, the spectra were fitted jointly. The figure also shows how the BAT and XRT hardness ratios and spectra evolve over time. A general softening trend can be seen across both bands, though the data harden during the flares, as is typical (e.g. Golenetskii et al. 1983; Ford et al. 1995; Borgonovo & Ryde 2001; Goad et al. 2007; Page et al. 2007). This softening with time likely explains why there was no significant gamma-ray emission detected at the time of the second large flare seen by the XRT, just after $T_0 + 200$ s.

The flare around 100 s was detected over both gamma-ray (BAT and GBM) and X-ray bands, though; as mentioned in Section 2.3, there is only a slight hint of an increase in the UVOT *white* magnitude at this same time. Extracting and fitting simultaneous BAT and XRT spectra demonstrates that there is curvature between the gamma-ray and X-ray bands; this is also shown by the differences in the independent power-law fits shown in Fig. 6. Broken power-law models are preferred for spectra from both the rising and falling portions of the flare. The break energy is not well-constrained in either case, but is located towards the top end of the XRT bandpass (between ∼3–10 keV).

Instead of using a series of broken power laws to fit GRB light curves, an alternative method was proposed by O'Brien et al. (2006) and Willingale et al. (2007): the light curve is parametrized by one or two components each comprising an early exponential rise which then rolls over into a power-law decay. The first of these components accounts for the gamma-ray and early X-ray emission (the 'prompt' phase), while the second (which is not always seen – see fig. 2 of Willingale et al. 2007) forms what we typically see as the afterglow at later times. These components allow an intrinsically curved light curve to be fitted without relying on a series of abrupt breaks in a power-law model. Excluding the times where the flares are seen, this exponential-to-power-law model can easily account for the BAT–XRT light curve of GRB 080810. The second, 'afterglow' component begins to dominate in the interval 500–3500 s, between the end of the first and beginning of the second orbit of data. The optical data can also be modelled with the exponential-to-power-law combination. Using this model, the afterglow $E_{\rm iso}$ was calculated to be 1.6×10^{52} erg, approximately a 10th of the prompt $E_{\rm iso}$ (Section 2.1). As for the prompt measurement, this is also high, compared with typical values of 10^{51} for afterglows (Willingale et al. 2007).

Fig. 8 brings together all the photometric data considered in this paper, from the gamma-ray regime to radio wavelengths. The gamma-ray and X-ray light curves have been converted to flux densities by assuming simple power-law fits (changing over time where there is evidence for spectral evolution). Note that all light curves except the X-ray and radio points have been vertically offset from their actual positions, to avoid overlap and make the plot clearer.

The early high-energy photon index evolves from harder to softer, as indicated by the fact that the *Fermi* (8–1000 keV data from the summed NaI detectors, normalized to 100 keV) and BAT data extend till ∼100 s, while the softer, 1 keV XRT data show apparent prompt emission out to at least 400 s; at this time *Swift* entered the South Atlantic Anomaly and so stopped collecting data for the remainder of the orbit.

The exponential-to-power-law model fits (O'Brien et al. 2006; Willingale et al. 2007) to the BAT, XRT and *R*-band data are shown as solid lines in the figure, with the dotted sections showing the continuation of these models beyond the extent of the data. The model jointly fitted to the BAT–XRT data (with the BAT data extrapolated to 1 keV) is also shown as the higher dotted blue line; the 20 keV magenta line is the same model (though with a different normalization) as the joint BAT–XRT fit. Each optical band is initially consistent with the same slope ($\alpha_{\rm opt} = 1.22 \pm 0.09$ when the power-law decay takes over), with slightly different normalizations between the filters. Note that the second of the radio points is only a marginal detection, at the 2.4σ level.

The second component fitted to the X-ray and optical profiles also contains an exponential rise. Such an increase is usually assumed because the second component is expected to turn on some time after the prompt trigger; however, in this burst, the early *R*-band points actually show an initial increase, peaking at ∼100 s after the

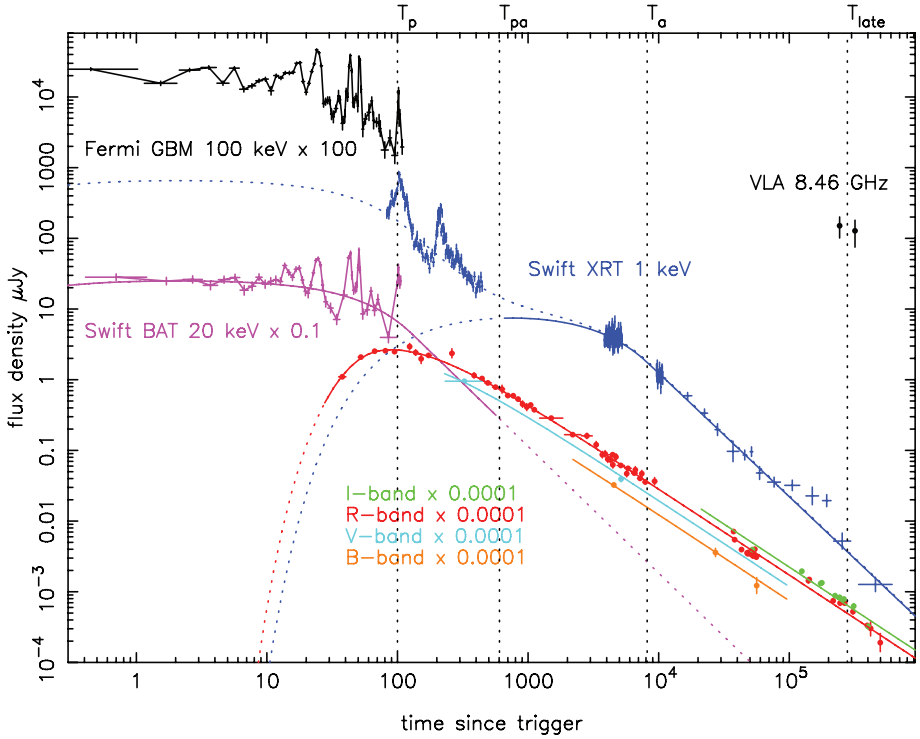

Figure 8. Multiwavelength flux density light curves, showing the gamma-ray, X-ray, optical and radio data collated for GRB 080810. Four fiducial times are marked by dotted vertical lines and curved lines indicate model fits; both sets of lines are explained in the text. With the exception of the X-ray and radio data, the light curves have been vertically offset to make the plot clearer; these offsets are given in the figure.

trigger, and provide us with a method of fitting the turn-on of the afterglow. With only three or four points between the initial *ROTSE* detection and the peak of the optical emission, however, quantifying the speed of the rise would be overinterpreting the data.

We do not have a detailed theoretical model for the onset of the afterglow with which to compare the data. It is possible that part of the rise seen could be caused by spectral evolution (that is, the passage of the peak of the spectrum through the bandpass), although it is reasonable to assume that we are mainly seeing an increase in peak flux as the external (afterglow) shock begins and strengthens, ∼30 s after the burst.

The vertical dotted lines mark four times at which spectral energy distributions (SEDs) have been created (Fig. 9): $T_{\rm p}$, at 50 s after the trigger, is during the prompt phase, where *Fermi*, BAT and *ROTSE*-III data are available; $T_{\rm pa}$ is the time at which the prompt and afterglow model fits are equal in X-ray flux (∼600 s after the trigger); $T_{\rm a}$ indicates the time at which the power-law decay starts in the X-ray band (∼8 ks); $T_{\rm late}$ is the point around which we have X-ray, optical and radio measurements (shortly before ∼300 ks). The optical flux values in Fig. 9 have been corrected for the Lyman forest absorption (Curran et al. 2008b) and the X-ray data corrected for the hydrogen column. The error bars on the optical points are smaller than the markers plotted.

The first SED, at $T_{\rm p}$, is a distinctly different shape from the later, afterglow-dominated plots. The prompt spectrum is shown as a cut-off power law (see Table 2) with the extension below the X-ray band shown by the curved dotted line, indicating that we assume this component peaks somewhere between the optical and X-ray bands since, as can be seen in Fig. 8, the optical emission at this time is totally dominated by the afterglow component. The power-law dotted line from the optical band at this time is parallel to the optical–X-ray slope at $T_{\rm pa}$ – i.e. it represents the afterglow component. There is no evidence for a prompt optical flash (caused by reverse shock emission), since this should be brighter than an extrapolation of the (forward shock) X-ray spectrum. The inferred break between the X-ray and optical bands will be due to synchrotron self-absorption, ν_a. Shen & Zhang (2009) discuss how to constrain the location of the emission region from the self-absorption frequency in a prompt optical-to-gamma-ray SED, assuming the optical and gamma-ray emission are both from the same synchrotron continuum. Their equations give an approximate range of $5 < R$ ($10^{14}\Gamma_{300}^{3/4}B_4^{1/4}$ cm) <16 (for $\nu_{\rm a} > \nu_{\rm opt}$) for the radial distance of the prompt emission from the centre of the GRB explosion. Here, Γ is the bulk Lorentz factor ($\Gamma = 300 \times \Gamma_{300}$) and B is the magnetic field strength ($B = B_4 \times 10^4$ G). This distance is of the same order as that estimated by Kumar et al. (2007).

Yost et al. (2007) discuss a number of GRBs where optical observations were obtained during the burst, but prompt optical emission was not detected, as we believe is the case for GRB 080810. They compare the optical-to-gamma-ray spectral indices ($\beta_{\rm opt-\gamma}$) with the gamma-ray spectral slopes (β_γ) and find that most of their values imply that there is a spectral rollover between the optical and higher frequencies. The numbers for GRB 080810 at time $T_{\rm p}$ ($\beta_{\rm opt-\gamma} \sim 0.53$ and $\beta_\gamma \sim 0.7$) are entirely consistent with their measurements. It seems likely that these events are part of the same population as GRBs with prompt optical detections, but are at the faint end of the distribution.

There is no significant evolution of the X-ray spectral index over the entire period $T_{\rm pa}$ to $T_{\rm late}$, with $\beta_{\rm X} = 1.00 \pm 0.09$. The optical spectral index also remains constant until at least $T_{\rm a}$, with $\beta_{\rm opt} = 0.51 \pm 0.22$ (from a comparison of the R, v and b measurements at $T_{\rm a}$). Thus, we find $\Delta\beta$ across the break is ∼0.5 as expected for a cooling break, although the uncertainties on the β values are large.

The SED at $T_{\rm pa}$ has been created using only the apparent afterglow flux for the X-ray data – the lower of the blue lines in Fig. 8. At this time, the spectral break must be at or below the optical band

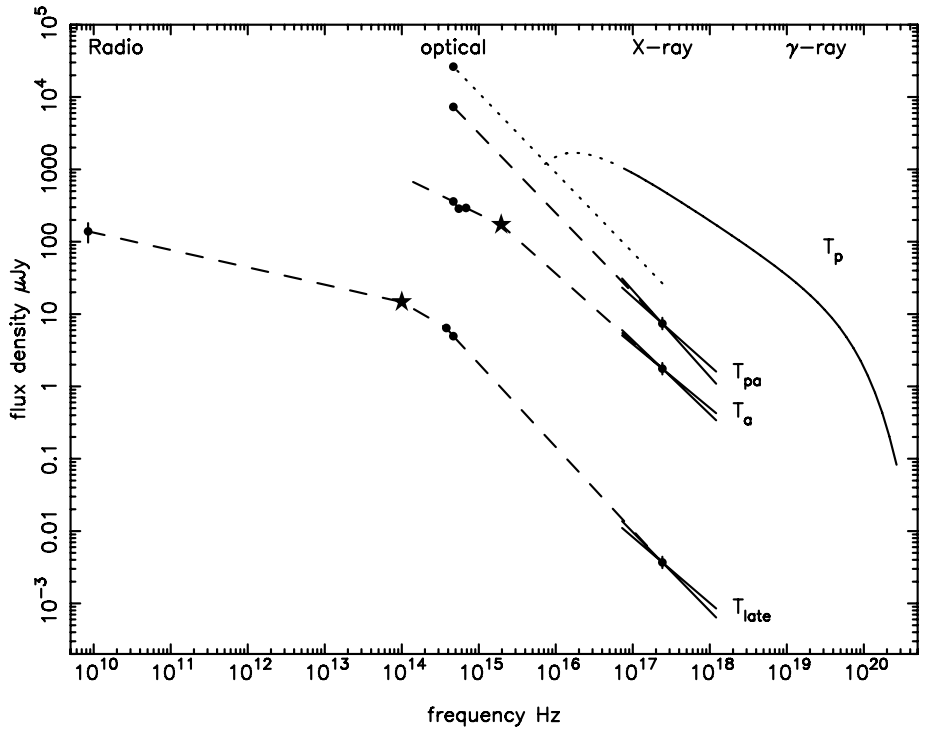

Figure 9. SEDs of GRB 080810 at the times of the vertical lines in Fig. 8. The stars indicate the approximate (cooling) break frequencies for the third and fourth SEDs. See text for details.

because the optical flux clearly lies on the direct extrapolation of the X-ray spectrum. Between $T_{\rm pa}$ and $T_{\rm a}$, the X-ray temporal decay is slow, while the optical has already passed into the power-law phase; that is, the X-ray decay starts later and is then more rapid than in the optical [$\alpha_{\rm X} = 1.81 \pm 0.20$ compared to $\alpha_{\rm opt} = 1.22 \pm 0.09$; we note that, using this method of parametrizing the light curve, $\alpha_{\rm X}$ is slightly steeper than – though consistent with – the value obtained from the series of broken power laws (see Table 3)]. Even including the contribution from the residual prompt component (i.e. using the flux from the joint BAT-XRT model – the upper dotted blue line in Fig. 8), the X-ray data still decay more gradually than the optical over this time frame.

As an aside, we note that Granot, Ramirez-Ruiz & Perna (2005) find that a structured jet could lead to a steeper decay in the optical than in the X-ray – the opposite of the measurements for GRB 080810. Using the standard fireball closure relationships (e.g. Zhang & Mészáros 2004), the optical data at this time are consistent with a wind medium undergoing slow cooling, with $\nu_{\rm m} < \nu < \nu_{\rm c}$. In this case, $\alpha = (3\beta + 1)/2 = [(3 \times 0.51) + 1]/2 = 1.27$, compared to the measured value of $\alpha_{\rm opt} \sim 1.22$.

The most straightforward way to explain this difference in the X-ray and optical behaviour is to have the cooling break moving towards higher frequencies (i.e. moving from the optical towards the X-ray). If the blastwave is indeed moving through a wind medium, then the cooling break is expected to increase with time as $t^{1/2}$. This would, however, necessitate a transition from a wind to a homogeneous medium for the break then to move down to lower frequencies (see later), which would lead to a change in the optical decay which is not clearly seen. An alternative explanation for the movement of the cooling break to higher energies is energy injection. Using the equations for the luminosity index, q, given by Zhang et al. (2006), we find that this part of the decay is indeed consistent with energy injection (that is, $q < 0$). The approximate frequency of this cooling break is marked by a star in Fig. 9; it cannot be determined accurately because of the lack of constraint on the optical index, but lies within the range 10^{15}–2×10^{16} Hz.

BVRI data from OSN at 50 ks after the trigger (the closest measurements were taken and then extrapolated to this exact time by using the slope of the light curve) provide a spectral slope of $\beta_{\rm opt} = 0.98 \pm 0.38$, consistent with the X-ray data; this confirms that the cooling break has passed through the optical frequencies by $T_{\rm late}$ and the data are consistent with the relevant closure relation [$\alpha = (3\beta - 1)/2$ for $\nu > \nu_{\rm c}$] within the uncertainties. As the cooling break moves through the optical band, we would expect to see a change in slope of the light curve; however, we do not have sufficient coverage or statistical precision at this late time to confirm or deny such a break. Furthermore, such a change in slope is likely to be spread over a decade in time, since the spectral break is a smooth, rather than abrupt, transition. With no radio index and the lack of measurements between the optical and radio regimes, it is not possible to say where the peak of the spectrum lies. The star again marks an approximate position for the break, although we note that there will be multiple breaks in this part of the spectrum, corresponding to this cooling break, the peak frequency and the synchrotron self-absorption frequency. The radio data are consistent with the extrapolation of a synchrotron spectrum from the optical and X-ray bands, though.

The optical spectral measurements are quite poorly constrained, both at early and late times and, within the errors, $\beta_{\rm opt}$ could be consistent with a constant value from $T_{\rm late}$ to $T_{\rm a}$. We also note that the X-ray data during the power-law decay ($\beta_{\rm X} = 1.00 \pm 0.09$ and $\alpha_{\rm X} = 1.81 \pm 0.20$) are not consistent with being above $\nu_{\rm c}$ (specifically, the temporal slope is too steep and is, in fact, steeper than is typical for a pre-jet-break slope; see, e.g. Evans et al. 2009), indicating the decay may not be governed by the standard fireball model (e.g. Rees & Mészáros 1992; Mészáros & Rees 1994, 1997; Sari, Piran & Narayan 1998) with a single synchrotron emission component. This lack of agreement with the standard fireball model appears to be the case for a growing number of afterglows, with many bursts for which we have good, multiwavelength data presenting challenges which still need to be accounted for (e.g. Willingale et al. 2007; GRB 061007 – Schady et al. 2007; Mundell et al. 2007; GRB 061121 – Page et al. 2007).

There is no evidence for a jet break (Rhoads 1999) in the data out to at least 6 d (which is within the range of *Swift* jet break times discussed by Racusin et al. 2009). This places a limit on the jet opening angle of $\theta_{\rm j} > 4^\circ$ (Sari, Piran & Halpern 1999; Frail et al. 2001) and, hence, a lower limit on the total gamma-ray energy, $E_\gamma > 8 \times 10^{50}$ erg. The beaming fraction, $E_\gamma / E_{\rm iso}$, is therefore >0.0027, which is of the same order as the those found for the samples in Frail et al. (2001) and Bloom, Frail & Kulkarni (2003).

The so-called canonical XRT light curve (Nousek et al. 2006; Zhang et al. 2006) typically starts with a steep decay, with $\alpha \sim 3$, which is generally attributed to off-axis emission, often referred to as the 'curvature effect' (Fenimore, Madras & Nayakshin 1996; Kumar & Panaitescu 2000; Dermer 2004). However, the early X-ray light curve of GRB 080810 shows a significantly slower decline, with $\alpha \sim 1$. In fact, the beginning of the GRB 080810 light curve is very similar to that of GRB 060607A (Molinari et al. 2007; Ziaeepour et al. 2008), both in X-rays and the optical: X-ray flares, superimposed on a relatively slow decline, while the optical emission rises smoothly, independently of the variability seen by the XRT and BAT. Both bursts also show low $N_{\rm H\,I}$. This slower-than-expected decay could be (at least partly) caused by repeated flaring on top of the underlying continuum. Alternatively, there could be input from the X-ray afterglow; the optical afterglow has clearly risen by this time (with little evidence of prompt emission; Fig. 8), but the X-ray light curve cannot be fully deconvolved into the prompt and afterglow components.

No plateau phase is seen in the optical data – the emission rises and then fades steadily away – which could be explained by the lack of a strong optical component during the prompt phase: from the exponential-to-power-law model, the plateau phase often seen in the X-ray may be a consequence of the bright prompt emission dominating at early times as the afterglow emission rises (see, e.g. Page et al. 2009 for an example of this). The final optical decay starts around 300 s, while the X-ray plateau extends to ∼8 ks before the onset of the power-law decay. These findings (the optical data showing no plateau and beginning the power-law decay phase earlier) were also noted for GRB 061121 (Page et al. 2007), another burst for which good, multiband data were obtained.

3.3.2 *Onset of the afterglow*

Measurement of the peak time of the afterglow component in the optical band gives us the opportunity to calculate the initial Lorentz factor, Γ_0 (Molinari et al. 2007). Estimating the peak to occur at ∼100 s (from the *ROTSE*-III data), and taking $E_{\rm iso}$ to be 3×10^{53} erg, Γ_0 is found to be $\sim 640 (\eta_{0.2}\, n_0)^{-1/8}$ (for a constant density medium), at the high end of the range of estimates from other bursts (Molinari et al. 2007; Page et al. 2009; Rykoff et al. 2009). Here, η is the radiative efficiency and n is the particle density of the surrounding medium in cm^{-3}. However, there is some evidence that the data are better suited to a wind environment, rather than constant density,

model. In this case, $\Gamma_0 \sim 235(\eta_{0.2})^{-1/4}$, taking $A = 3 \times 10^{35}$ cm^{-1}, where the number density, $n(r) = Ar^{-2}$ (Chevalier & Li 2000; Molinari et al. 2007).

Zhang, Kobayashi & Mészáros (2003) and Jin & Fan (2007) discuss the possible appearance of the reverse shock in optical light curves. These papers consider three types of reverse shock emission: Type I light curves show both forward- and reverse-shock emission peaks; Type II shows a single peak, corresponding to the reverse shock, with a later flattening caused by the forward shock as it starts to dominate the emission; Type III light curves show no sign of the reverse shock, with just a single rise and fall of the optical emission. The light curve of GRB 080810 appears to be a member of this third class, with a single power-law decay seen from around 100 s until several hundred kiloseconds after the burst trigger. The synchrotron frequency, $\nu_{\rm m}$, at the time the reverse shock crosses the outflow is therefore very small, well below the optical band.

Panaitescu & Vestrand (2008) found an anticorrelation between the peak optical flux and the time of the peak for fast-rising optical afterglows. K-correcting our values to the fiducial redshift of $z = 2$ used by Panaitescu & Vestrand gives a peak time of ∼85 s and a corresponding peak flux of ∼94 mJy, meaning that the optical afterglow of GRB 080810 is consistent with their findings. This correlation is explained by a structured outflow being seen off-axis.

Although the rise seen in the optical light curve is naturally explained as the onset of the afterglow, there are other possible mechanisms – for example, off-axis or structured outflows or two-component jets (e.g. Granot et al. 2002). These other explanations are discussed for a sample of *Swift*–UVOT bursts by Oates et al. (2009). They find that the onset of the forward shock or an off-axis viewing angle could best explain the rises seen in the light curves.

3.3.3 *Flares*

Prior to *Swift*, X-ray observations tended to start hours or days after the burst trigger, with only a few light curves showing flaring activity (Piro et al. 1998, 2005). However, flares are now regularly detected by the XRT (see Chincarini et al. 2007; Falcone et al. 2007 for survey papers), with about 50 per cent of *Swift* bursts showing them, typically in the first thousand seconds or so (Burrows et al. 2007; Chincarini et al. 2007). Some light curves, however, do show rebrightenings at later times (e.g. GRB 050502B – Falcone et al. 2006; GRB 050724 – Campana et al. 2006; GRB 070710A – Covino et al. 2008; GRB 070311 – Guidorzi et al. 2007; see also Kocevski, Butler & Bloom 2007). Confirming the interpretation established by Burrows et al. (2005b) and Zhang et al. (2006), Curran et al. (2008a) investigated late-time flares, finding that their properties are consistent with those of early ones, implying that the central engine may sometimes be active for up to 100 ks or that it can be restarted. In the case of the deviation from the power-law decay at about 150 ks in the light curve of GRB 080810 presented here, the $\Delta t/t$ and $\Delta F/F$ values are within the range of the values plotted in Fig. 3 of Curran et al. for their sample of late-time flares. Because of the uncertainties on the values, this particular flare could be consistent with internal shocks ($\Delta t/t < 1$), refreshed shocks or patchy shells (see Ioka et al. 2005. Both the early and late flares seen here lie within the distribution of $\Delta t/t$ found by Chincarini et al. (2007).

4 SUMMARY AND CONCLUSIONS

Plentiful broad-band data were collected for the bright GRB 080810 which triggered both *Swift* and *Fermi*. The redshift was found to be 3.355 ± 0.005, and the burst was energetic, with an isotropic energy of 3×10^{53} erg in the prompt emission component and 1.6×10^{52} erg in the afterglow. There is no evidence for a jet break up to 6 d after the burst occurred.

The prompt component (detected from 0.3–10^3 keV) is seen to evolve from hard to soft, with $E_{\rm peak}$ decreasing from ∼600 to ∼40 keV over 110 s. Despite being detected at the same time as the gamma-ray emission, the optical data appear to be strongly dominated by the afterglow, with little (if any) prompt component. SEDs created at fiducial times during the observations show the movement of the cooling break with time. By $T_{\rm a}$ (8 ks after the burst), the break frequency has moved from the optical band towards the X-rays, lying in the range 10^{15} to 2×10^{16} Hz; at later times ($T_{\rm late} \sim$ 300 ks), this cooling break has evolved to $< 3 \times 10^{14}$ Hz. Although the optical data conform to the standard fireball interpretation, the decay of the X-ray afterglow (after about 10^4 s) is too rapid to be consistent with the model.

Well-sampled bursts such as GRB 080810 enable us to investigate more thoroughly the myriad of models which exist for GRBs, with the ultimate goal of a complete and consistent description of GRB emission from early to late times.

ACKNOWLEDGMENTS

The authors gratefully acknowledge support for this work at the University of Leicester by STFC, in Italy by funding from ASI and at PSU by NASA contract NAS5-00136. ER thanks the NOVA-3 network for support. JXP is partially supported by NASA/*Swift* grant NNX07AE94G. *ROTSE*-III has been supported by NASA grant NNG-04WC41G and the Australian Research Council and ESR would like to thank the TABASGO Foundation. AJvdH was supported by an appointment to the NASA Postdoctoral Program at the MSFC, administered by Oak Ridge Associated Universities through a contract with NASA. FY was supported by NASA Swift Guest Investigator grants NNG-06GI90G and NNX-07AF02G. The DARK cosmology centre is funded by the DNRF. This paper is partly based on observations made with the Nordic Optical Telescope, operated on the island of La Palma jointly by Denmark, Finland, Iceland, Norway and Sweden, in the Spanish Observatorio del Roque de los Muchachos of the Instituto de Astrofisica de Canarias. This work is partly based on observations with the INT, operated on the island of La Palma by the Isaac Newton Group in the Spanish Observatorio del Roque de los Muchachos of the Instituto de Astrofisica de Canarias. We also thank P. Chandra and D. Frail for help with the radio data, G. Marcey and D. Fischer for scheduling the ToO during their Keck observing time, Peter Jonker for performing the INT/WFC observations and C. Thöne for working on the data from the NOT and Danish telescope. We extend our thanks to the whole of the *Fermi*-GBM team for their work on this new mission. Finally, we thank the anonymous referee for their detailed comments, which improved the paper.

REFERENCES

Adelman-McCarthy J. K. et al., 2008, ApJS, 175, 297
Akerlof C. et al., 2003, PASP, 115, 132
Arnaud K. A., 1996, in Jacoby G., Barnes J., eds, ASP Conf. Ser. Vol. 101, Astronomical Data Analysis Software and Systems V. Astron. Soc. Pac., San Francisco, p. 17
Band D. et al., 1993, ApJ, 413, 281
Barth A. J. et al., 2003, ApJ, 584, L47
Barthelmy S. D. et al., 2005, Space Sci. Rev., 120, 143
Bloom J. S., Frail D. A., Kulkarni S. R., 2003, ApJ, 594, 674

Borgonovo L., Ryde F., 2001, ApJ, 548, 770
Burenin R. et al., 2008, GCN Circ., 8088
Burrows D. N. et al., 2005a, Space Sci. Rev., 120, 165
Burrows D. N. et al., 2005b, Sci, 309, 1833
Burrows D. N. et al., 2007, Phil. Trans. R. Soc. A, 365, 1213
Campana S. et al., 2006, A&A, 454, 113
Chandra P., Frail D., 2008, GCN Circ., 8103
Chevalier R. A., Li Z.-Y., 2000, ApJ, 536, 195
Chincarini G. et al., 2007, ApJ, 671, 1903
Covino S. et al., 2008, MNRAS, 388, 347
Curran P. A., Starling R. L. C., O'Brien P. T., Godet O., van der Horst A. J., Wijers R. A. M. J., 2008a, A&A, 487, 533
Curran P. A., Wijers R. A. M. J., Heemskerk M. H. M., Starling R. L. C., Wiersema K., van der Horst A. J., 2008b, A&A, 490, 1047
Dermer C., 2004, ApJ, 614, 284
de Ugarte Postigo A., Thöne C. C., Hjorth J., Jakobsson P., Banhidi Z., Grundahl F., Arentoft T., 2008a, GCN Circ., 8089
de Ugarte Postigo A., Aceituno F., Castro-Tirado A. J., 2008b, GCN Circ., 8090
Evans P. A. et al., 2009, MNRAS, 397, 1177
Falcone A. D. et al., 2006, ApJ, 641, 1010
Falcone A. D. et al., 2007, ApJ, 671, 1912
Fenimore E. E., Madras C. D., Nayakshin S., 1996, ApJ, 473, 998
Ford L. A. et al., 1995, ApJ, 439, 307
Frail D. A. et al., 2001, ApJ, 562, L55
Fynbo J. P. U. et al., 2005, ApJ, 633, 317
Gehrels N. et al., 2004, ApJ, 611, 1005
Ghisellini G., Celotti A., Lazzati D., 2000, MNRAS, 313, L1
Goad M. R. et al., 2007, A&A, 468, 103
Golenetskii S. V., Mazets E. P., Aptekar R. L., Ilinskii V. N., 1983, Nat, 306, 451
Granot J., Panaitescu A., Kumar P., Woosley S. E., 2002, ApJ, 570, L61
Granot J., Ramirez-Ruiz E., Perna R., 2005, ApJ, 630, 1003
Grupe D., Nousek J. A., Vanden Berk D. E., Roming P. W. A., Burrows D. N., Godet O., Osborne J., Gehrels N., 2007, AJ, 133, 2216
Guidorzi C., Steele I., Tanvir N., 2008, GCN Circ., 8093
Guidorzi C., Bersier D., Tanvir N., 2008, GCN Circ., 8099
Guidorzi C. et al., 2007, A&A, 474, 793
Holland S. T., Page K. L., 2008, GCN Circ., 8095
Ikejiri Y., Uemura M., Ohsugi T., Kawabata K., Arai A., Yamanaka M., Sakimoto K., 2008, GCN Circ., 8081
Ioka K., Kobayashi S., Zhang B., 2005, ApJ, 631, 429
Jakobsson P. et al., 2006, A&A, 460, L13
Jin Z. P., Fan Y. Z., 2007, MNRAS, 378, 1043
Kocevski D., Butler N., Bloom J. S., 2007, ApJ, 667, 1024
Kumar P., Panaitescu A., 2000, ApJ, 541, L51
Kumar P. et al., 2007, MNRAS, 376, L57
Lazzati D., Morsony B. J., Begelman M. C., 2009, ApJ, submitted (arXiv:0904.2779v1)
Mallozzi R. S., Preece R. D., Briggs M. S., 2005, RMFIT: A Lightcurve and Spectral Analysis Tool. Univ. Alabama, Huntsville
Meegan C. A. et al., 2008, GCN Circ., 8100
Meegan C. A. et al., 2009, ApJ, 702, 791
Mészáros P., Rees M. J., 1994, MNRAS, 269, L41
Mészáros P., Rees M. J., 1997, ApJ, 476, 232
Molinari E. et al., 2007, A&A, 469, L13
Mundell C. G. et al., 2007, ApJ, 660, 489
Nousek J. A. et al., 2006, ApJ, 642, 389
Oates S. R. et al., 2009, MNRAS, 395, 490
O'Brien P. T. et al., 2006, ApJ, 647, 1213
Page K. L. et al., 2007, ApJ, 663, 1125
Page K. L. et al., 2008a, GCN Circ., 8080
Page K. L., Holland S. T., Palmer D. M., Barthelmy S. D., Burrows D. N., Roming P. W. A., Gehrels N., 2008b, GCN Report 157
Page K. L. et al., 2009, MNRAS, 395, 328
Panaitescu A., Vestrand W. T., 2008, MNRAS, 387, 497
Pe'er A., Ryde F., Wijers R. A. M. J., Mészáros P., Rees M. J., 2007, ApJ, 664, L1
Piro L. et al., 1998, A&A, 331, L41
Piro L. et al., 2005, ApJ, 623, 314
Poole T. S. et al., 2008, MNRAS, 383, 627
Preece R. D., Briggs M. S., Mallozzi R. S., Pendleton G. N., Paciesas W. S., Band D. L., 1998, ApJ, 506, L23
Prochaska J. X., Chen H.-W., Bloom J. S., 2006, ApJ, 648, 95
Prochaska J. X., Chen H.-W., Dessauges-Zavadsky M., Bloom J. S., 2007, ApJ, 666, 267
Prochaska J. X., Perley D., Howard A., Chen H.-W., Marcy G., Fischer D., Wilburn C., 2008, GCN Circ., 8083
Racusin J. L. et al., 2009, ApJ, 698, 43
Rees M. J., Mészáros P., 1992, MNRAS, 258, 41
Rhoads J. E., 1999, ApJ, 525, 737
Romano P. et al., 2006, A&A, 456, 917
Roming P. W. A. et al., 2005, Space Sci. Rev., 120, 95
Ryde F., 2004, ApJ, 614, 827
Ryde F., Pe'er A., 2009, ApJ, 702, 1211
Rykoff E. S., 2008, GCN Circ., 8084
Rykoff E. S. et al., 2009, ApJ, 702, 489
Sakamoto T. et al., 2008a, GCN Circ., 8082
Sakamoto T. et al., 2008b, GCN Circ., 8101
Sakamoto T. et al., 2009, ApJ, 693, 922
Sari R., Piran T., Narayan R., 1998, ApJ, 4997, L17
Sari R., Piran T., Halpern J. P., 1999, ApJ, 519, L17
Savchenko V., Neronov A., 2009, MNRAS, 396, 935
Schady P. et al., 2007, MNRAS, 380, 1041
Shen R.-F., Zhang B., 2009, MNRAS, in press
Stamatikos M., Sakamoto T., Band D. L., 2008, in Huang Y.-F., Dai Z.-G., Zhang B., eds, AIP Conf. Proc. 1065, Nanjing Gamma-Ray Burst Conference. Am. Inst. Phys., New York, p. 59
Starling R. L. C. et al., 2008, MNRAS, 384, 504
Thöne C. C., de Ugarte Postigo A., Liebig C., 2008, GCN Circ., 8106
Vogt S. S. et al., 1994, SPIE, 2198, 362
von Kienlin A. et al., 2004, SPIE, 5488, 763
Willingale R. et al., 2007, ApJ, 662, 1093
Yost S. A. et al., 2007, ApJ, 669, 1107
Zhang B., Mészáros P., 2004, Int. J. Mod. Phys. A, 19, 2385
Zhang B., Kobayashi S., Mészáros P., 2003, ApJ, 595, 950
Zhang B., Fan Y. Z., Dyks J., Kobayashi S., Mészáros P.Burrows D. N., Nousek J. A., Gehrels N., 2006, ApJ, 642, 354
Ziaeepour H. et al., 2008, MNRAS, 385, 453

This paper has been typeset from a TEX/LATEX file prepared by the author.